The Pennsylvania State University

The Graduate School

DEVELOPMENT OF AN ALL AQUEOUS THERMALLY REGENERATIVE AMMONIA BATTERY USING CU(I,II) REDOX REACTIONS

A Thesis in

Energy and Mineral Engineering

by

Renaldo E. Springer

Submitted in Partial Fulfillment
of the Requirements
for the Degree of

Master of Science

May 2022

The thesis of Renaldo E. Springer was reviewed and approved by the following:

Derek M. Hall

Undergraduate Program Chair of Energy Engineering

Thesis Adviser

Serguei Lvov

Professor of Energy and Mineral Engineering and Materials Science and Engineering

Christopher A. Gorski

Associate Professor of Civil and Environmental Engineering

Mort D. Webster

Professor of Energy Engineering

Associate Department Head for Graduate Education

Disclaimer: The content of this thesis was originally published in The Journal of Electrochemical Society and is referenced as: R. Springer, N.R. Cross, S.N. Lvov, B.E. Logan, C.A. Gorski, D.M. Hall, An All-Aqueous Thermally Regenerative Ammonia Battery Chemistry Using Cu(I, II) Redox Reactions, J. Electrochem. Soc. 168 (2021) 070523. https://doi.org/10.1149/1945-7111/AC1030.

Abstract

Thermally regenerative ammonia batteries (TRABs) are electrochemical energy conversion devices that convert low-grade waste heat into electrical power. The formation of metal amine complexes during cell discharge, resulting from the addition of ammonia to the anolyte, generates electrical power. After cell discharge, the ammonia is recovered from the spent anolyte by distillation with low-grade waste heat and re-added to the former cathode chamber, repeating the process. To date, TRABs suffer from poor performance due to their reliance on dissolution and deposition redox reactions with transition metals. Here, we present a new TRAB chemistry utilizing Cu(I/II) redox reactions; in conjunction with ligands to stabilize the aqueous copper ions, thereby creating the first reported all-aqueous TRAB. Rotating disc electrode studies were conducted to evaluate thermodynamic and kinetic parameters of prospective anolyte and catholyte chemistries. The use of NH_3(aq) and Br^-(aq) ligands resulted in a cell potential difference of 695 ± 2 mV with rate constants of 101 ± 5 μm s^{-1} and 819 ± 236 μm s^{-1}, respectively. Single cell tests achieved power densities up to 350 W m^{-2} which are the highest reported for single metal TRABs at 25 °C. Coulombic efficiencies exceeded 90% and their energy storage densities were two to four times of those reported for alternative TRAB chemistries.

Contents

List of Figures

List of Tables

List of Nomenclature

English Letters:

A	Electrode area
b	Molality
c_{ox}	Oxidation species concentration
c_{red}	Reduction species concentration
E_{eq}	Equilibrium potential
E_{cell}	Cell potential
E_{w}	Working electrode potential
E^0	Standard Equilibrium Potential
f	Frequency
F	Faraday's constant
$\Delta_f G^0$	Standard Gibbs energy of formation
$\Delta_r G^0$	Standard Gibbs energy of reaction
j	Current density
j_{cell}	Cell current density
$j_{lim,a}$	Anodic limiting current density
$j_{lim,a}$	Cathodic limiting current density
j_0	Exchange current density
j^o_0	Standard exchange current density
k_o	Electrochemical rate constant
R	Molar gas constant
R_{ct}	Charge transfer resistance
R_s	Solution resistance
T	Thermodynamic temperature
ν_n	Cu(I) ligand Stoichiometric coefficient
ν_m	Cu(II) ligand Stoichiometric coefficient
Z_r	Real area-specific impedance
Z_i	Imaginary area-specific impedance
Z_M	Modulus area-specific impedance

Greek Letters:

α_c	Transfer coefficient
β_n	Cu(I) stability constant
β_m	Cu(II) stability constant
η	Electrode overpotential

Acknowledgements

The beginning of every new journey can be daunting, but I am grateful to have had an amazing support team to help me along this journey through graduate school. Therefore, I would like to thank Serguei Lvov, Bruce Logan, Christopher Gorski, Tim Duffy, Nicholas Cross, and Akash Ganesh for making the transition into research an easy and enjoyable experience. I would also like to give special thanks to my mentors, Derek Hall, and Jonathan Matthews, for igniting my passion for research. I will forever be indebted to you, and I cannot give enough thanks for the endless hours of coaching, your wisdom, and guidance; you will forever be appreciated. To my family, thanks to all of you for your unconditional love and support.

This work was partially supported by a seed grant from the Penn State Institutes of Energy and the Environment and by a grant under DE-FE0032030.

Chapter 1 - Introduction

1.1 Background and motivation

Sustainable energy generation and efficiency is an increasingly important topic as the world approaches a critical phase in preventing further increases in temperature across the globe. As renewable technologies such as wind and solar improve, the coupling of equally capable energy storage systems to minimize the associated intermittency is in high demand. However, current energy storage technologies rely heavily on expensive materials and components, hindering viable large-scale applications. Therefore, researchers are looking to exploit new sources for electricity on demand that do not increase carbon emissions, like waste heat, to provide ancillary services for the electric grid to aid in a smooth transition to a low-carbon society. Waste heat is a byproduct of many industrial and natural processes, from manufacturing and electricity generation to geothermal activity. This waste heat is characterized based on its temperature, with low-grade waste heat (temperature <130 °C) accounting for more than 60% of the total waste heat emitted.[7] As a mostly untapped energy source, low-grade waste heat equates to approximately half of the U.S. current energy demand (2.94×10^{13} kWh in 2019).[8] Harvesting a fraction of this low-grade waste heat would alleviate CO_2 emissions from the combustion of additional fossil fuels, thereby promoting a more sustainable energy infrastructure.[1,2,9,10] However, there is vast room for improvement as most heat recovery technologies struggle with poor performance and scalability.[1,9,11]

Viable technologies for the conversion of low-grade waste heat to electricity must have competitive power and energy densities, as well as ease of scalability.[12] Solid-state thermoelectric devices, such as the thermoelectric generator (TEG), can convert heat flux to electric power based on the Seebeck effect,[13,14] but; high manufacturing costs and low power densities hinder practical applications.[9,15,16] Liquid-based thermoelectric cells are better candidates for efficiently harvesting waste heat due to more appealing costs and scalability.[17] However, with power densities ranging from 0.5 to 12 W m^{-2}, feasible implementation of these technologies is hindered due to low power generation and efficiency.[2,16] Previous research has shown

that of these heat recovery technologies, thermally regenerative ammonia batteries (TRABs) are the most promising due to their relatively high power densities and Carnot efficiency.[18]

TRABs are hybrid flow batteries where electrolyte solutions, stored in external tanks, are pumped into the cell stack where redox reactions occur. Unlike alternative approaches to waste heat recovery, TRABs can store harvested thermal energy by using ammonia as an energy carrier.[1] During TRAB cell discharge, dissolution of the metal anode due to oxidation releases metal amine complexes into the anolyte, whereas aqueous metal ions deposit at the cathode in the absence of ammonia.[2] Thermal recovery of the potential difference is accomplished by separating ammonia from the depleted anolyte through distillation and re-introducing the recovered ammonia to the former cathode chamber, regenerating the potential difference.[1,2,19] Thereby creating a closed-loop cycle using heat as an input, stored in the energy carrier (ammonia), providing electric energy as an output. Although TRABs are a promising option for converting waste heat into electric power compared to competing technologies, they still have issues, such as low energy storage densities and poor coulombic efficiencies.[1,2,4]

1.2 Literature Review

1.2.1 Cell Design

Cell design is a significant consideration to the development of TRABs, due to the impact of ohmic resistances on overall cell performance. In electrochemical systems, mass transfer phenomena impact the rate of electrochemical reactions.[20] Primarily, the two cell configurations previously used to assess the performance of a TRAB were a closed batch system and a flow system.[21] The working electrochemical principles between these two designs are the same. The flow TRAB differs only in operation as a continuous flow rather than a batch-fed system, allowing for a more compact design as the electrodes, spacers, and membranes are close.[22] This compact design effectively increased electrode surface area per volume while decreasing the distances between the electrodes. The first Cu-TRAB developed was initially tested in batch reactors, where relatively large distances between the copper mesh electrodes resulted in high ohmic

resistances and a low power density of 25 W m^{-2} (normalized to membrane area).[22] The conversion from batch reactors to flow TRABs improved both the energy and power densities, 45 W m^{-2} (normalized to membrane area), of the cell.[23] This flow cell design has become common in recent years as TRABs continue to develop, with a more focused interest in improving electrolyte solutions and membrane performance.

The properties of the electrode material and the membrane also significantly impact cell performance. Electrode porosity results in an increased surface area and higher theoretical power output, albeit while increasing the mass transfer resistance.[24] However, using a flow system mitigates this associated increase in mass transfer resistance by enhancing reactant distribution in the TRAB.[24] Membrane thickness and selectivity (AEM versus CEM) can also impact the power density due to its ion transfer efficiency, species cross-over, and membrane resistance.[25]

1.2.2 Single-metal TRABs

The first Cu-TRAB developed utilized copper mesh electrodes with copper nitrate and ammonia nitrate salts, in which ammonia acted as the ligand in the anolyte.[26] The added ammonia produced ammine complexes as shown in the redox half-reactions below[27]:

$$\text{Cathode: } Cu^{2+}(aq) + 2e^- \rightarrow Cu^0(s) \qquad E^0 = +0.34\ V \qquad [1]$$

$$\text{Anode: } Cu(NH_3)_4^{2+}(aq) + 2e^- \rightarrow Cu^0(s) + 4\ NH_3(aq) \qquad E^0 = -0.03\ V \qquad [2]$$

where E^0 is the standard reduction potential (vs. SHE). Although the power density was significantly larger than previous thermoelectric devices, there were significant drawbacks due to its reliance on deposition and dissolution reactions. During cell operation, low anodic coulombic efficiency limited its viability as a closed-loop system.[3] The high anodic dissolution rate resulted in net losses per cycle, ultimately depleting the copper anode and consuming the platinum cathode electrode.[22] Improving upon the Cu-TRAB,

researchers have developed a silver TRAB that utilizes carbon electrodes to avoid metal dissolution losses into the electrolyte.[28] The potential difference between the anodic and cathodic redox reactions for the Ag-TRAB are much larger when compared to the Cu-TRAB half-cell reactions[27]:

$$\text{Cathode: } Ag^{+}\,(aq) + e^{-} \rightarrow Ag^{0}\,(s) \qquad E^{0} = +0.80\ \text{V} \qquad [3]$$

$$\text{Anode: } Ag(NH_3)_2^{+}\,(aq) + e^{-} \rightarrow Ag^{0}\,(s) + 2\,NH_3\,(aq) \qquad E^{0} = +0.37\ \text{V} \qquad [4]$$

Using carbon electrodes, the Ag-TRAB achieved 100 discharge cycles with minimal decay, surpassing previous TRABs, which averaged less than ten cycles, indicating strong cell reversibility.[28] The increased potential difference between the redox reactions, compared to the Cu-TRAB, also improved cell power densities by 64%. However, one major drawback of the Ag-TRAB, among other grid-scale flow battery technologies, is the use of precious metals as its redox-active metal (cobalt, lithium, vanadium), making scalability difficult.[29,30]

1.2.3 Bi-metallic TRABs

Bimetallic TRABs have made huge advancements towards increased cell power densities by maximizing the potential difference between the redox couples. Researchers coupled two relatively inexpensive redox metals, copper, and zinc, to create a new TRAB with the highest power density reported in the literature.[31] The Cu/Zn-TRAB produced power densities of 723 ± 45 W m^{-2} at 40 °C with a linear temperature relationship of 12.25 W m^{-2} $°C^{-1}$.[31] However, dendrite formation and cell self-discharge, due to ion crossover, affected performance significantly at high temperatures. Energy storage density is also an important metric in determining the viability of batteries. The Ag-based and Cu-based TRABs use active species concentrations between 0.1 to 0.2 M with equilibrium potential differences between 0.4 to 0.45 V,[21,28] resulting in energy storage densities between 1 to 3 Wh L^{-1}. The Cu/Zn bimetallic TRAB, although having a high power density, had an energy storage density of 0.635 Wh L^{-1} with 0.1 M active species

concentrations.[31] One disadvantage of the Cu/Zn-TRAB is the reliance on an external low voltage source during the charging phase, which ultimately decreases the net energy output.[32]

1.2.4 All-aqueous TRAB

In this study, we use non-volatile ligands to bypass the reliance on deposition/dissolution reactions. Metal-ligand coordination bonding has previously stabilized reactive intermediates and improved the reactivity of catalytic reactions.[33] The thermodynamic stability of these metal-ligand complexes can be predicted using a combination of the hard/soft principle of acids and bases, the chelation effect, and the ligand field stabilization energy.[34,35] Based on these principles, Cu(I) preferentially bonds with soft donors, while Cu(II) favors more borderline donors.[36] The three ligands of interest, NH_3(aq), Cl^-(aq), and Br^-(aq), were selected based on ligand field strength, ranging from strong to weak.[37] Therefore, the instability of Cu(I) in oxidizing environments[38] can be circumvented, allowing for the use of the Cu(I, II) redox reactions.

These metal-ligand bonds also change the cathodic and anodic electrode potentials. In essence, this new technology pairs redox reactions between aqueous metal complexes with the same metal center, instead of metal deposition/dissolution reactions, as seen in the half-reactions below:

$$\text{Cathode: } Cu(Br)_4^{2-}(aq) + e^- \rightleftharpoons Cu(Br)_3^{2-}(aq) + Br^-(aq) \qquad E^0 = +0.52\ V \qquad [5]$$

$$\text{Anode: } Cu(NH_3)_4^{2+}(aq) + e^- \rightleftharpoons Cu(NH_3)_3^{+}(aq) + NH_3(aq) \qquad E^0 = +0.04\ V \qquad [6]$$

In doing so, this technology dramatically improves the potential difference of previous Cu-TRABs while avoiding deposition/dissolution complications. The reliance on aqueous electroactive species combines the recharging advantages of TRABs[39] with the performance benefits of an all-vanadium redox flow battery (VRFB), a common electroactive species used in redox flow batteries.[40] Similar to previous TRABs, the discharge is electrochemical, and the thermal charging process requires the separation of a volatile ligand from an aqueous solution.[3,26,28]

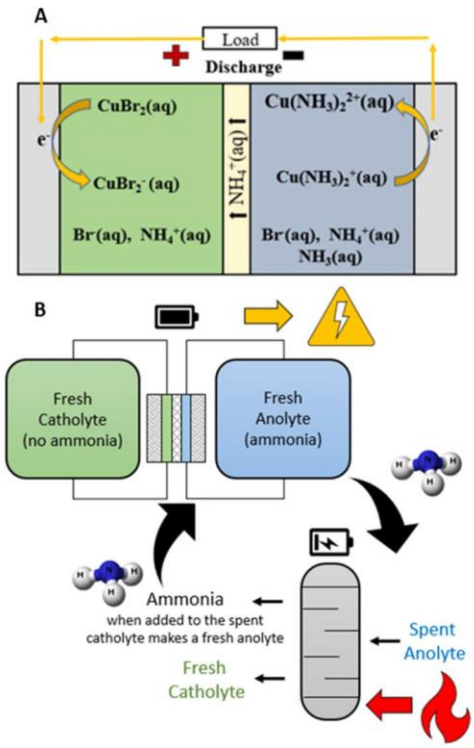

Figure 1. Electric discharge (A) and thermal charging process (B) for the all-aq TRAB.

For this study, rotating disc electrode (RDE) experiments quantified the impact of the three ligands (Br^-, Cl^-, NH_3) on the electrochemical parameters for the Cu(I, II) redox reaction. The peak power densities and coulombic efficiencies of this new TRAB chemistry, analyzed in full-cell tests, were quantified with a conventional zero-gap flow battery system with graphite felt electrodes.

Chapter 2 – Materials, Methods, and Calculations

2.1 Experimental Approach

Electrolyte solutions were prepared using ammonium chloride (99.5% Alfa Aesar), ammonium bromide (99% Alfa Aesar), and copper chloride dihydrate (99% Alfa Aesar) salts. Ammonium hydroxide was prepared from a 28 % wt. ammonia Alfa Aesar stock solution. The chemical conversion of Cu(II) complexes to Cu(I) was carried out under an argon gas blanket (99.998% Praxair), following a procedure developed previously.[41,42] Briefly, an electrolyte containing Cu(II) complexes with a ligand that stabilizes

the formation of Cu(I) is circulated with Cu(s) (99.9% Alfa Aesar metal basis), promoting the formation of Cu(I) complexes through the consumption of Cu(s) and Cu^{2+}(aq).

Analysis of ligand impacts on the electrochemical parameters of the Cu(I, II) redox couple was conducted using a Pine Instruments rotating disc electrode (RDE) system and a multiport glass cell (#AKCELL2). The RDE test system consisted of an Ag/AgCl reference electrode (RE) with a 4 mol kg^{-1} KCl(aq) reference solution, and the counter electrode (CE) was a platinum coil. The two working electrodes used were platinum (Pt) and glassy carbon (GC) Fixed-Disk RDE Tips (Pine Instruments), both having a surface area of 0.1964 cm^2.

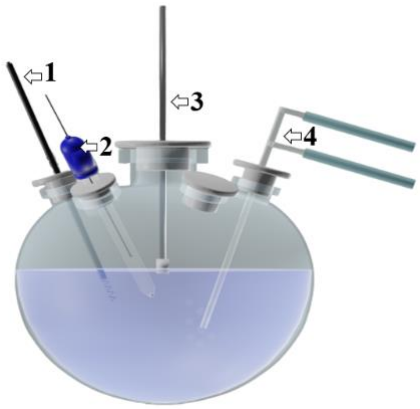

Figure 2. RDE multiport glass cell used for aqueous Cu(I, II) redox analysis at 25 ^{o}C and 1 bar: (1) Coiled-wire platinum counter electrode (CE); (2) Ag(s)/AgCl(s) reference electrode (RE); (3) RDE with working electrode (WE); (4) argon gas inlet and outlet.

Both working electrodes were polished with an alumina polishing solution (0.05 µm Buehler) on a microfiber felt and rinsed with deionized (DI) water before each test. All RDE tests were performed using 10×10^{-3} mol kg^{-1} Cu(I) species and 10×10^{-3} mol kg^{-1} Cu(II) species. Ligand concentrations were varied between 1 and 4 mol kg^{-1}.

The full-cell performance studies used a zero-gap flow battery cell. The zero-gap cell had machined graphite plates with 5 cm^2 serpentine flow channels, steel end plates, carbon cloth electrodes, ion-conductive membranes, and fluorosilicone gaskets.

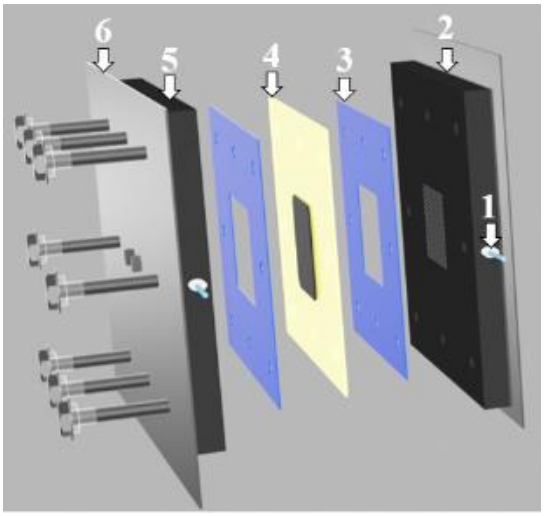

Figure 3. Model of RFB used for full cell testing: (1) electrolyte inlet and outlet; (2) negative electrode current collector; (3) fluorosilicone gasket; (4) ion-conductive membrane with carbon cloth electrodes; (5) positive electrode current collector; (6) steel endplate.

The membranes examined were Nafion 117 (183 μm thick), Nafion 115 (127 μm thick), and a Fumasep FAPQ-375-PP anion exchange membrane (68-82 μm thick) (AEM). The electrolytes were pumped using two Masterflex diaphragm pumps with a combination of perfluoroalkoxy (PFA) and polytetrafluoroethylene (PTFE) tubing and fittings. The electrolyte solutions were pumped at a constant flow rate (200 mL min^{-1}) into the cell through the flow channels then back into 1-liter reservoir tanks. In all full-cell tests, the positive electrode electrolytes contained 5 mol kg^{-1} NH_4Br with Cu(I, II) bromide complexes, and the negative electrode electrolytes contained 5 mol kg^{-1} NH_4Br and 5 mol kg^{-1} NH_3 with Cu(I, II) ammonia complexes. Initial copper concentrations for both positive and negative electrolytes were 0.5 mol kg^{-1}. The initial state of charge (SOC) was controlled through the mixing of Cu(I) with Cu(II) solutions, using an approach developed in a previous study for the CuCl-HCl electrolyzer.[43–45]

Experimental measurements were performed with a Gamry Reference 600 for RDE tests and a Gamry Reference 3000 for full-cell tests. The tests consisted of open circuit potential (OCP), linear sweep voltammetry (LSV), and electrochemical impedance spectroscopy (EIS) measurements. RDE LSV data were collected with a scan rate of 10 mV s^{-1} from potentials ± 0.3 V vs. OCP, while full-cell LSV data were obtained using a scan rate of 5 mV s^{-1}. LSV data collected from the RDE system were corrected for the solution resistance, obtained via EIS, to examine the overpotential (η) contributions from electrode reaction processes. EIS tests used a frequency range of 0.1 Hz to 100 kHz, sampling every 5 points per decade with a 10 mV root mean square (RMS) alternating current perturbation around the OCP. Tests were conducted around OCP to minimize non-linear kinetic responses at applied potentials. Cycling tests were performed at a constant current of 4 mA cm^{-2} with potential limits of 1 and 0.5 V.

2.2 Calculations

2.2.1 Thermodynamics

Cell thermodynamics were calculated using a series of equations in conjunction with thermodynamic databases. Using stability constants (β) for each copper-ligand complex, the standard values of the electrode potentials, E^0, were calculated for the Cu(I, 0) (used to determine region of Cu(I) stability) and Cu(I, II) redox reactions (**Equations 7** and **8**) where L is the ligand molecule, z is the charge number of the ligand, and n and m are the stoichiometric coefficients of the ligands in the Cu(I) and Cu(II) complexation reactions, respectively.

$$Cu(L)_n^{(1+nz)}(aq) + e^- \rightleftharpoons Cu(s) + nL^z(aq) \quad [7]$$

$$Cu(L)_m^{(2+mz)}(aq) + e^- \rightleftharpoons Cu(L)_n^{(1+nz)}(aq) + (m-n)L^z(aq) \quad [8]$$

The new values ($E^0_{Cu(I)L/Cu}$ and $E^0_{Cu(II)L/Cu(I)L}$) were calculated from the standard E^0 values reported in the CRC electrochemical series[46] ($E^0_{Cu(II)/Cu(I)}$= 0.153 V vs. SHE and $E^0_{Cu(I)/Cu}$ = 0.342 V vs. SHE), and the stability constants, β_n and β_m, for the $Cu(I)L_n$ and $Cu(II)L_m$ reactions.

$$E^0_{Cu(I)L/Cu} = E^0_{Cu(I)/Cu} - \frac{RT}{F}\ln(\beta_n) \quad [9]$$

$$E^0_{Cu(II)L/Cu(I)L} = E^0_{Cu(II)/Cu(I)} + \frac{RT}{F}\ln(\beta_n\,\beta_m^{-1}) \quad [10]$$

where F=96485 C mol^{-1} is Faraday's constant, R=8.314 J mol^{-1}K^{-1} is the molar gas constant, and T is the thermodynamic temperature in Kelvin.

The stability constants for Cu(I, II) molal complexes were obtained from literature based on complexation reactions shown in **Table 1**.[47–49]

Table 1. Metal-ligand complexation reactions for Cu(I, II) aqueous species.

	Chloride	**Bromide**	**Ammonia**
Cu(I)	$Cu^+ + Cl^- = CuCl^0$ $CuCl^0 + Cl^- = CuCl_2^-$ $CuCl_2^- + Cl^- = CuCl_3^{2-}$	$Cu^+ + Br^- = CuBr^0$ $CuBr^0 + Br^- = Cu(Br)_2^-$ $Cu(Br)_2^- + Br^- = Cu(Br)_3^{2-}$	$Cu^+ + NH_3 = Cu(NH_3)^+$ $Cu(NH_3)^+ + NH_3 = Cu(NH_3)_2^+$ $Cu(NH_3)_2^+ + NH_3 = Cu(NH_3)_3^+$
Cu(II)	$Cu^{2+} + Cl^- = CuCl^+$ $CuCl^+ + Cl^- = CuCl_2^0$ $CuCl_2^0 + Cl^- = CuCl_3^-$ $CuCl_3^- + Cl^- = CuCl_4^{2-}$	$Cu^{2+} + Br^- = CuBr^+$ $CuBr^+ + Br^- = Cu(Br)_2^0$ $Cu(Br)_2^0 + Br^- = CuBr_3^-$ $CuBr_3^- + Br^- = CuBr_4^{2-}$	$Cu^{2+} + NH_3 = Cu(NH_3)^{2+}$ $Cu(NH_3)^{2+} + NH_3 = Cu(NH_3)_2^{2+}$ $Cu(NH_3)_2^{2+} + NH_3 = Cu(NH_3)_3^{2+}$ $Cu(NH_3)_3^{2+} + NH_3 = Cu(NH_3)_4^{2+}$ $Cu(NH_3)_4^{2+} + NH_3 = Cu(NH_3)_5^{2+}$

These complexation reactions were then used in a system of equations to determine the ligand speciation concentrations, providing insight into the effect of ligand concentrations on the distribution of species at ambient conditions. Example **Equations 11-16** highlight the computation of the complexation reactions

associated with Cu^{2+} and the chloride ligand. In these calculations, activity coefficients ($\gamma_{\pm}$) were assumed to be equal to one to simplify calculations.

$$K_1 = \frac{\gamma_{\pm} b_{CuCl^+}}{\gamma_{\pm} b_{Cu^{2+}}\ \gamma_{\pm}\ b_{Cl^-}} \quad [11]$$

$$K_2 = \frac{\gamma_{\pm} b_{CuCl_2}}{\gamma_{\pm} b_{CuCl^+}\ \gamma_{\pm} b_{Cl^-}} \quad [12]$$

$$K_3 = \frac{\gamma_{\pm} b_{CuCl_3^-}}{\gamma_{\pm} b_{CuCl_2}\ \gamma_{\pm} b_{Cl^-}} \quad [13]$$

$$K_4 = \frac{\gamma_{\pm} b_{CuCl_4^{2-}}}{\gamma_{\pm} b_{CuCl_3^-}\ \gamma_{\pm} b_{Cl^-}} \quad [14]$$

Mass Balance Equations:

$$\Sigma b_{Cl^-} = b_{Cl^-} + b_{CuCl^+} + 2b_{CuCl_2} + 3b_{CuCl_3^-} + 4b_{CuCl_4^{2-}} \quad [15]$$

$$\Sigma b_{Cu^{2+}} = b_{Cu^{2+}} + b_{CuCl^+} + b_{CuCl_2} + b_{CuCl_3^-} + b_{CuCl_4^{2-}} \quad [16]$$

Accounting for the activity coefficients will impact calculated values; however, as the electroactive species' concentrations are on the milli-molal scale, the impact is deemed to be minuscule. Previous studies included activity coefficients in the potential calculations, and the resulting potentials changed by a few percent, but it did not change the trends observed substantially.[41,50] **Tables 2 and 3** show the **e**quilibrium constants for the Cu(I) and Cu(II) redox species used in these calculations.

Table 2. The equilibrium constants for the Cu(I)-ligand aqueous complexes.

K_{eq}	Chloride[41]	Bromide[51]	Ammonia[48]
1	1.34E+04	3.39E+03	5.50E+05
2	2.06E+01	2.14E+02	9.12E+04
3	2.03E-01	3.72E+00	6.30E-01

Table 3. The equilibrium constants for the Cu(II)-ligand aqueous complexes.

K_{eq}	Chloride[41]	Bromide[52]	Bromide[53]	Ammonia[54]	Ammonia[55]
1	2.51E+00	1.42E+01	4.79E+05	7.25E+05	1.20E+04
2	8.13E-02	3.97E-02	3.63E+01	8.17E+06	3.00E+03
3	2.51E-02	-	4.79E+00	3.75E+04	8.00E+02
4	5.01E-03	-	3.70E-01	6.06E+03	1.20E+02
5	-	-	-	1.19E+01	3.00E-01

2.2.2 Kinetics

Cell electrochemical kinetics for the Cu(I, II) complexation reactions were analyzed using data collected from electrochemical impedance spectroscopy (EIS) and linear sweep voltammetry (LSV). The Randles cell equivalent circuit for a rotating disc electrode, which accounts for the combination of ohmic resistance in series, $R_{s,}$ finite-length Warburg impedance, W_{s1}, constant phase element, CPE ($CPE_{1\text{-}T}$ and $CPE_{1\text{-}P}$)[43], and the charge transfer resistance, R_{ct}[5], was used to quantify how ligands influence the charge transfer process (**Figure 4**).

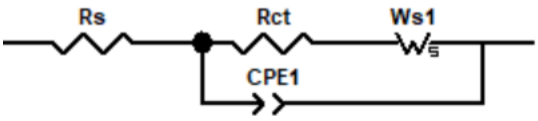

Figure 4. Randles Equivalent Circuit Model

Ligand effects on R_{ct} were converted to exchange current density (j_0) values, which are proportional to R_{ct} values obtainable through a Randle cell model. Equivalent circuit predictions (**Figure 5**) closely matched the experimental data supporting the use of a Randle circuit model.

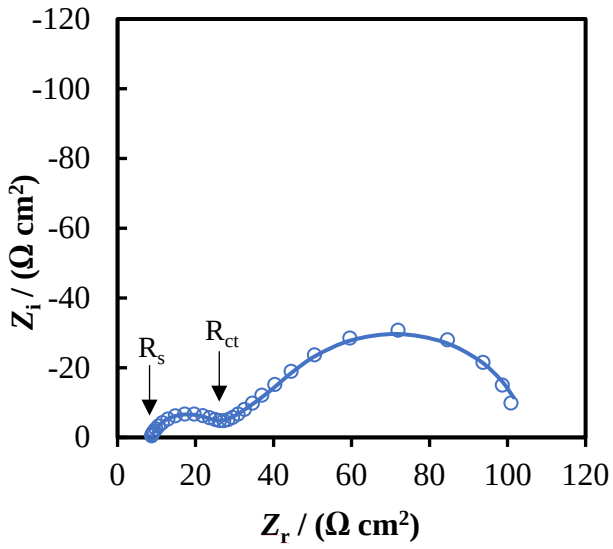

Figure 5. EIS data (circles) and equivalent circuit fitting (lines) of RDE data for Pt working electrode. Conditions: 500 RPM, 1 mol kg^{-1} NH_4Cl(aq), 25 °C and 1 bar.

The Randles cell equivalent circuit produces values based on the curve fit, an example of which is shown in **Table 4**, where W_R, W_P, and W_T are parameters for the Warburg element.

Table 4. Circuit model values used to fit the EIS spectra shown for the Pt working electrode. Conditions: 500 RPM, 1 mol kg^{-1} NH_4Cl(aq), 25 °C and 1 bar.

Circuit Element	Pt Surface
R_s / Ω	8.59 ± 0.05
R_{ct} / Ω	17.76 ± 0.16
W_R / Ω	75.64 ± 0.48
W_T	0.57 ± 0.01
W_P (fixed)	0.50
$CPE_{1\text{-}T}$ / F	4.10E-05 ± 0.29E-5
$CPE_{1\text{-}P}$	0.78 ± 0.01

Using EIS and the Randle cell circuit model, charge transfer resistances were used to calculate j_0 values[56] of the Cu(I, II) redox reaction for Pt and GC electrode surfaces. **Equation 17** relates R_{ct} to j_0, where A is the geometric electrode area.

$$j_0 = RT\,(FAR_{ct})^{-1} \quad [17]$$

The generalized Butler-Volmer (B-V) equation was used to determine the transfer coefficients (α_c) via the nonlinear fitting of LSV data using the Newton-Raphson method.[43,57]

$$j = \frac{[\exp(1-\alpha_c)(\frac{F\eta}{RT})]-[\exp(-\alpha_c)(\frac{F\eta}{RT})]}{(\frac{1}{j_0})+(\frac{1}{j_{lim,a}})\ [\exp(1-\alpha_c)\left(\frac{F\eta}{RT}\right)]-(\frac{1}{j_{lim,c}})\ [\exp(-\alpha_c)\left(\frac{F\eta}{RT}\right)]} \quad [18]$$

where j is the current density, $j_{lim,a}$ is the anodic limiting current density, $j_{lim,c}$ is the cathodic limiting current density and η is the overpotential, F is Faraday's Constant, R is the gas constant, T is the thermodynamic temperature, and α_c is the transfer coefficient. Values for $j_{lim,a}$ and $j_{lim,c}$ were obtained directly from the LSV plots, while j_0 values were obtained from EIS tests.

Rate constants (k_0) of the Cu(I, II) redox reactions were calculated using **Equation 19**[41], where c_{ox} and c_{red} are concentrations (mol cm^{-3}) of the oxidation and reduction species, respectively:

$$j_0 = Fk_0(c_{ox}^{1-\alpha c}c_{red}^{\alpha c}) \quad [19]$$

All potential values provided vs. SHE. The coulombic efficiency (ε_C) of the Br-NH_3 all-aq TRB was determined from a series of charge and discharge cycles at a constant current **(Equation 20)**[58]

$$\varepsilon_C = \frac{\int I\, dt_{charge}}{\int I\, dt_{discharge}} \quad [20]$$

where I is the cell constant current of charge and discharge for a time, t, between the potential limits, 0.5 to 1.0 V of the cycling tests. Theoretical energy storage density ($u_{,ideal}$) calculations were made following a simplified approximation which neglects potential cut-offs and activity coefficient effects[50] to compare the energy capacity of multiple TRAB chemistries:

$$u_{,ideal} = E^0_{cell} c_{total} F \quad [21]$$

where E^0_{cell} is the difference between the standard potentials of the redox reaction of interest in each half of the battery, and c_{total} is the molar concentration of the electroactive species limiting the state of charge.[50] For this TRAB chemistry, c_{total} is the total concentration of dissolved copper.

Chapter 3 – Results

3.1 Energy Storage Density

A thermodynamic analysis of the Cu(I, II) redox reaction with different ligands indicated that the full cell equilibrium potential of the new all-aq TRAB was significantly larger than single metal TRABs. Cu(I, II) equilibrium potentials (E_{eq}) were quantified through OCP measurements which showed a connection between E^0 and the participating metal-ligand complexes. The NH_3(aq) solutions resulted in negative E_{eq} shifts, whereas Br^-(aq) and Cl^-(aq) solutions resulted in positive E_{eq} shifts. Increases in ligand concentration also increased the extent of the potential shift, as seen in **Figure 6**.

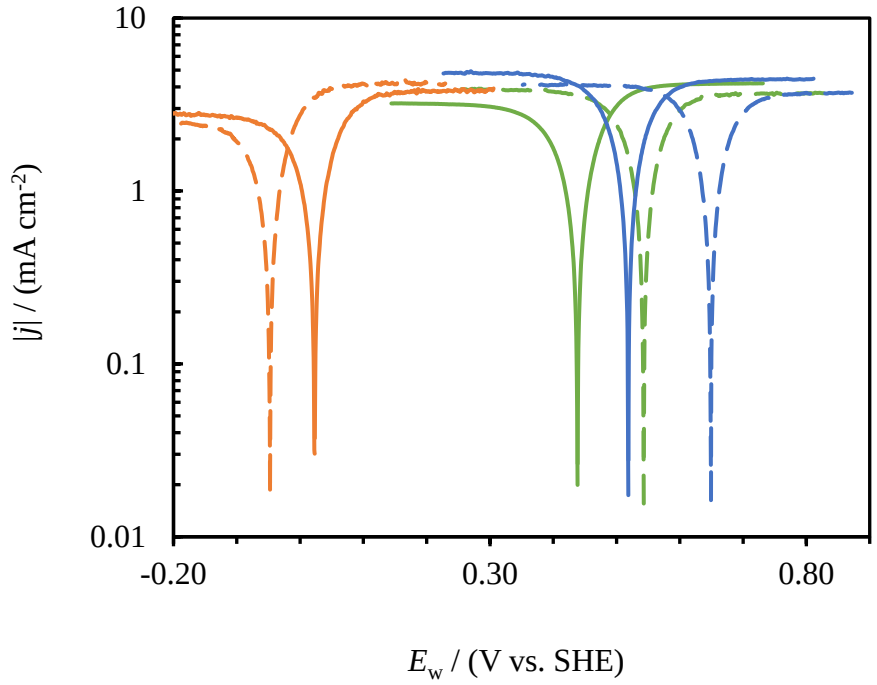

Figure 6. RDE LSV data highlighting the impacts of complexation on the Cu(I, II) redox reaction with 4 mol kg^{-1} (dashed lines) and 1 mol kg^{-1} (solid lines) solutions of NH_3(aq) (orange), NH_4Cl(aq) (green), and NH_4Br(aq) (blue). Conditions: 25 °C and 1 bar at 500 RPM.

The polarization curves obtained through LSV analysis indicated the limiting currents had minimal variation between ligands, relative to changes in j_0 and by relation k_0. The RDE potential of the working electrode is E_w (i.e., corrected for the solution resistance and reference electrode potential).

Speciation diagrams (**Figure 7**) were constructed using the equilibrium constants and the standard Gibbs energies at 25 °C and 1 bar to determine the species within the anolyte and catholyte. The speciation diagrams show that the dominant copper species complexes with more ligands as the ligand concentration increases in both the catholyte (copper bromide complexes) and anolyte (copper ammonia complexes) chambers.

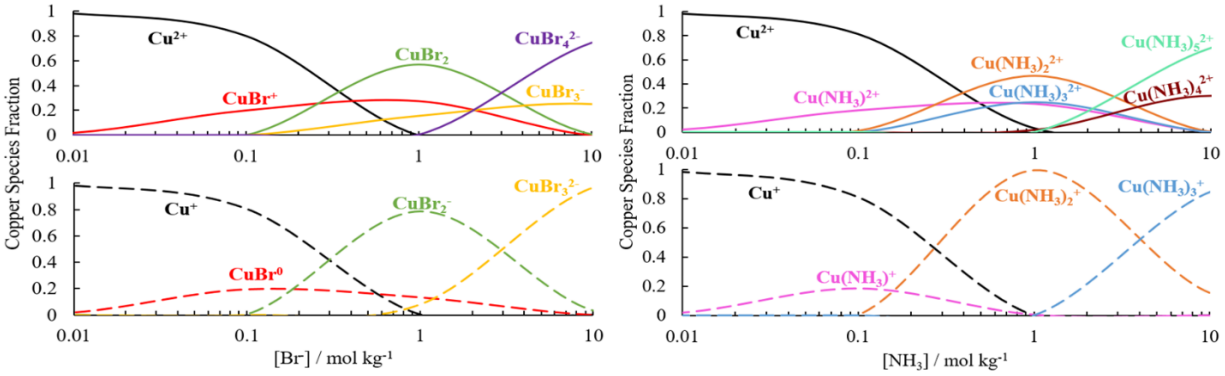

Figure 7. Fractional distribution of Cu(I, II)-Br and Cu(I, II)-NH_3 complexes as a function of total ligand concentration, at 25 °C and 1 bar with 0.5 mol kg^{-1} of total Cu.

Speciation analyses showed that Cl^-(aq) and Br^-(aq) ligands preferentially bonded to Cu(I) species while NH_3(aq) preferred Cu(II) species. Speciation calculations also show that these potentials can be predicted, with some accuracy, if the reaction stability constants or the standard Gibbs energy of all species are known for both Cu(I) and Cu(II) complexation reactions. This is shown in **Figure 8,** where calculated E_{eq}, determined using the Nernst equation, concentrations from the speciation analysis, and the standard thermodynamic values[41,59], is in relative agreement with the measured potentials.

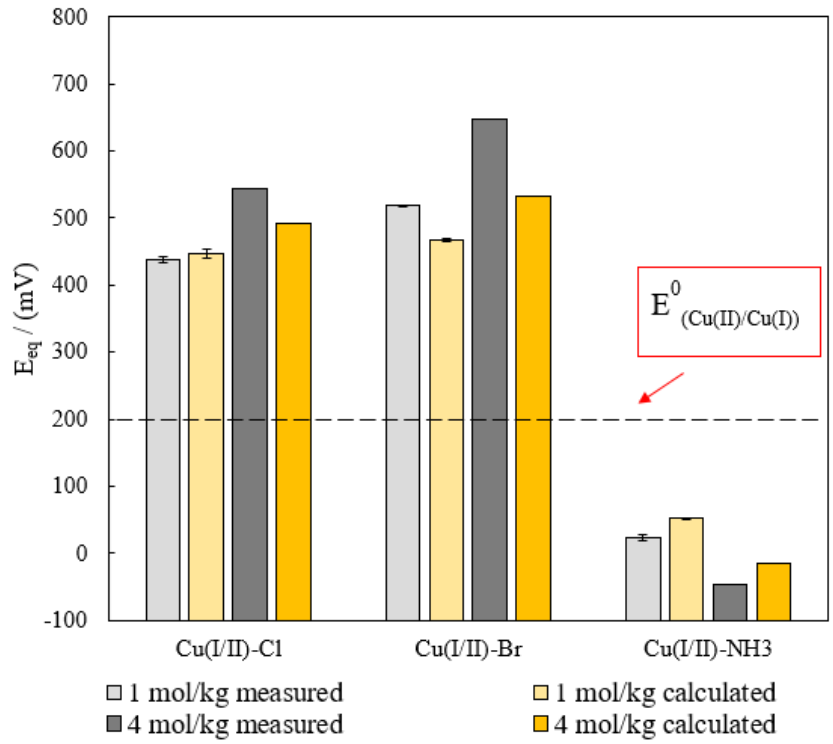

Figure 8. E_{eq} values of the Cu(I, II) redox reaction with different ligand types and ligand concentrations for an equimolal solution of Cu(I, II) species, where the dashed line is the standard reduction potential of the Cu(I, II) reaction in DI water.

Though speciation analyses generally agreed with experimental values obtained for both the Br^-(aq) and Cl^-(aq) species, Cu(II)-NH_3(aq) equilibrium constants from different sources[49,51–53,55,60,61] provided a large range of E_{eq} values suggesting some uncertainty surrounding the thermodynamic properties of Cu(II)-NH_3(aq) complexes. The use of **Eq. 10** indicated that E_{eq} can be further increased to 0.79 V with additional Br^-(aq) or decreased to −0.13 V[55] with additional NH_3(aq) by maximizing the extent of complexation.

Energy storage densities possible with the all-aq Cu-TRAB were also larger than those observed in previously published TRAB chemistries. With a standard cell potential of about 0.7 V and stable electroactive species concentrations of at least 0.5 mol kg^{-1} the energy storage density of the new TRAB was estimated to be at least 9.4 Wh L^{-1} using **Eq. 21**. This is considerably higher than the current values of 2.4 Wh L^{-1} from Cu-TRABs and 1.2 Wh L^{-1} from Ag-TRABs.[2]

3.2 Electrochemical Kinetics

The observed electrochemical kinetics of Cu(I, II) redox reactions were very fast compared to other prominent electrochemical energy conversion systems such as water electrolysis[56] and vanadium redox flow battery systems.[62] EIS was used to identify contributing mass and charge transfer resistances. Electrochemical kinetics and diffusion limitations were distinguished through their response to a changing diffusion layer thickness via RDE.[41] Varying rotation rates from 500 RPM to 2000 RPM dramatically decreased the low-frequency time constant (suggesting diffusion limitations) but did not impact the high-frequency time constant (indicating a surface reaction).

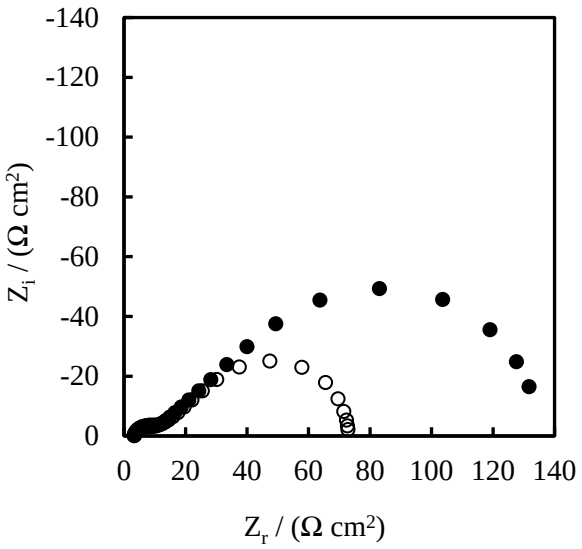

Figure 9. (a) Nyquist plots collected from an RDE using the Pt working electrode at 500 RPM (•) and 2000 RPM (○). Conditions: 4 mol kg^{-1} NH_4Cl(aq), 25 ^oC and 1 bar.

Equivalent circuit predictions (**Figure 10**) closely matched the experimental data supporting the use of a Randle circuit model. Changes in the R_{ct} value showed the impact of the surface material on the high-frequency semi-circle, indicating the reaction is faster on Pt relative to GC surfaces.

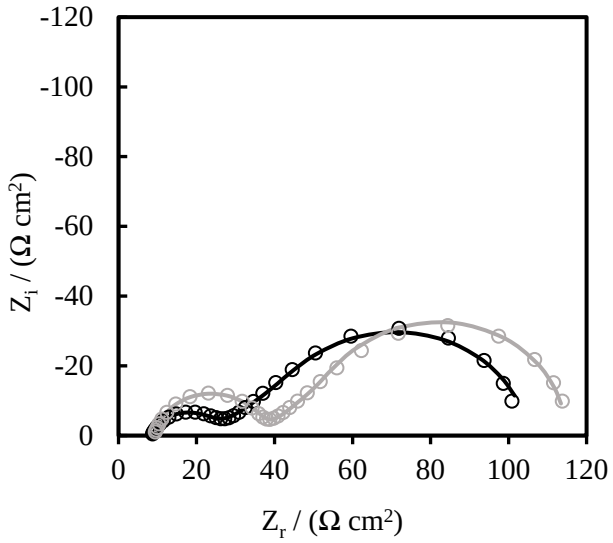

Figure 10. EIS data (circles) and fitting (lines) of RDE data for GC (grey) and Pt (black) working electrodes. Conditions: 500 RPM, 1 mol/kg NH_4Cl(aq), 25 ^oC and 1 bar.

EIS data (**Fig. 11**) from NH_3(aq), Br^-(aq), and Cl^-(aq) solutions were consistent with LSV data where the Cu(I, II) reactions were largely limited by mass transfer processes due to their fast kinetics. Hence, the diffusion layer thickness impacted limiting currents far more than differences between diffusion coefficients of the different complexes.

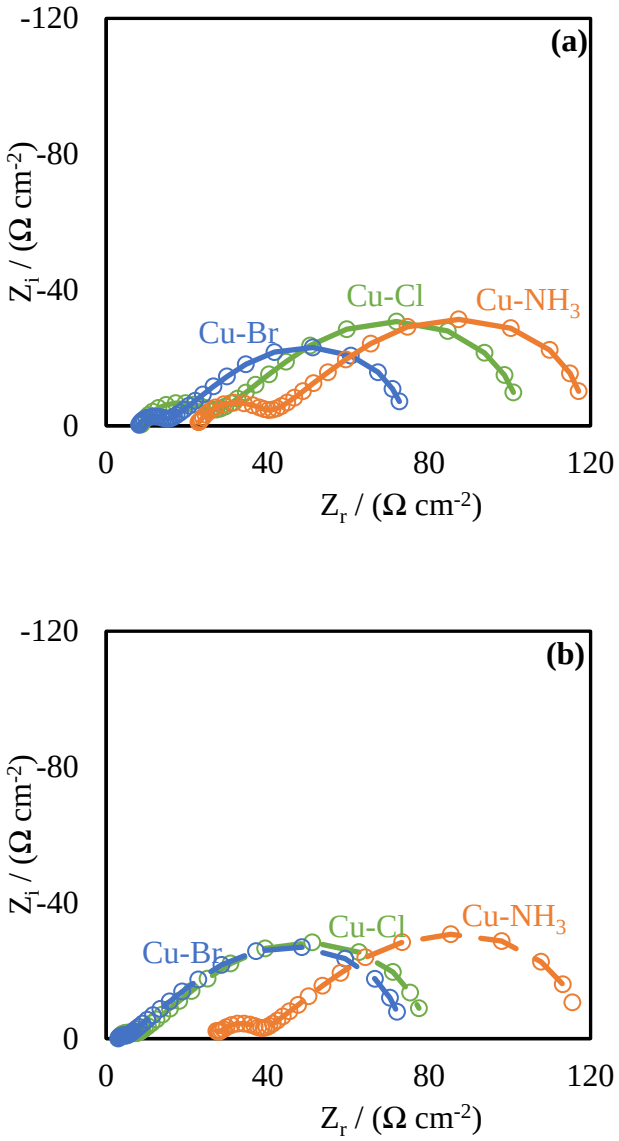

Figure 11. The effect of NH_3(aq), Cl^-(aq) and Br^-(aq) on the reaction kinetics and mass transfer sections of the impedance curves using the Pt working electrode at both (a) 1 mol kg^{-1}, (-), and (b) 4 mol kg^{-1}, (--), ligand concentrations. Conditions: 500 RPM, 25 ^{o}C and 1 bar.

Another observation was the small charge-transfer controlled regions of the Cu(I, II) reactions, indicating favorable kinetics, as little overpotential was required to reach the limiting current. Tafel analysis would ideally indicate symmetric polarization curves for both anodic and cathodic regions.[43] However, the small

charge-transfer region, indicative of facile kinetics, made Tafel and Koutecky-Levich analysis difficult. This is shown through a non-linear fitting, which indicated that transfer coefficients, α_c, still impacted the polarization curves. The influence of α_c can be seen if values of α_c are varied from 0.3 to 0.8 as the resulting curves deviate from the experimentally obtained data in both cathodic and anodic regions (**Figure 12**).

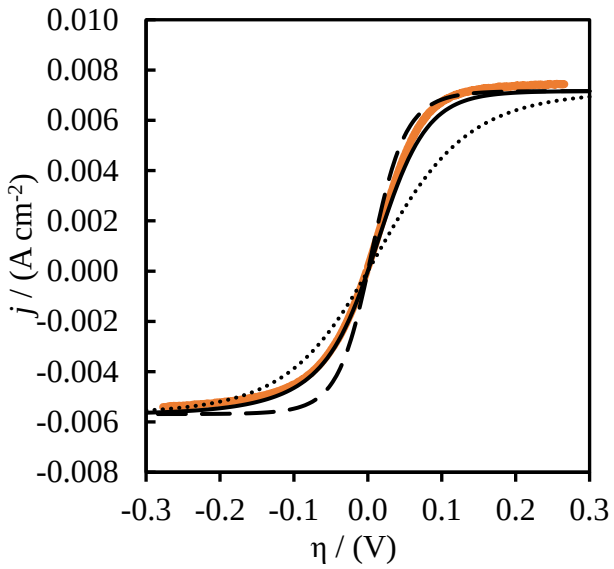

Figure 12. LSV data of Cu (I, II)-NH_3 complex data (orange) with a GC working electrode at 1 mol kg^{-1} NH_3(aq) and non-linear fitting results with **Equation 18** indicating α_c = 0.38 (solid black) and polarization curves from **Equation 18** assuming α_c = 0.3 (dashed) and 0.8 (dotted). Conditions: 2000 RPM, at 25 ^oC and 1 bar.

Overall, ligand concentration, ligand type, and surface materials only slightly changed α_c. Increasing the ligand concentration, consistently decreased the transfer coefficients, and for the most part, the coefficients were larger with GC *vs*. Pt. Unlike j_0 and E_{eq} values, no obvious trends were observed between the coefficients and ligand field strength (**Table 5**).

Table 5. Ligand complexation impact on the charge transfer coefficients of the Cu(I, II) redox reaction for Pt and GC working electrodes at 25 ^{o}C and 1 bar.

Ligand	b_L / mol kg^{-1}	$\alpha_{c,Pt}$ (± 1 %)	$\alpha_{c,GC}$ (± 1 %)
NH_3(aq)	1	0.34	0.38
	4	0.28	0.25
Cl^-(aq)	1	0.35	0.50
	4	0.30	0.48
Br^-(aq)	1	0.37	0.42
	4	0.30	0.33

The rate constants, k_0, were determined using EIS and LSV data analysis methods[44], indicating fast reaction kinetics with both Pt and GC electrodes (**Figure 13**). Rate constants were reported rather than exchange current densities as they are independent of anodic and cathodic species concentrations.

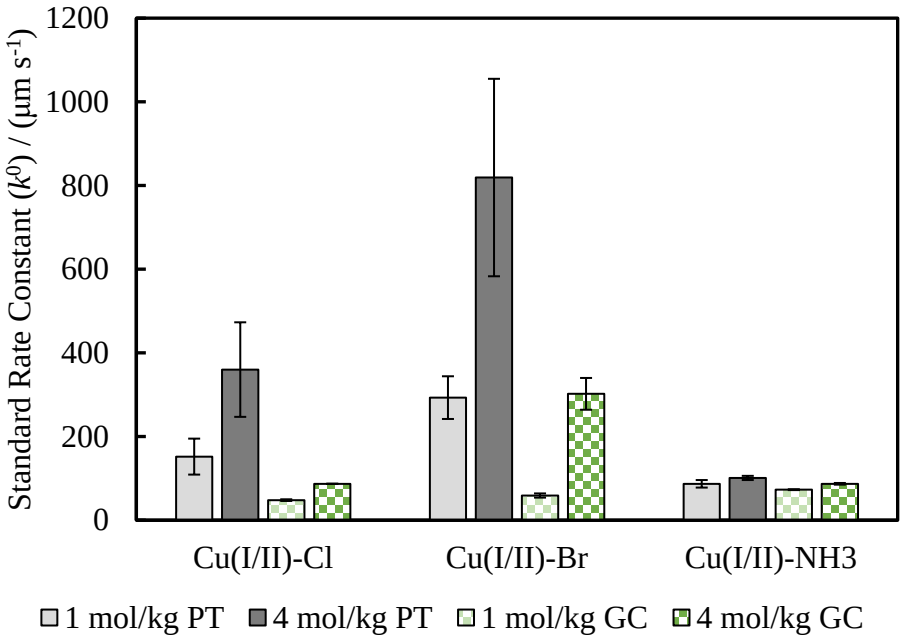

Figure 13. Ligand complexation impact on the k_0 of the Cu(I, II) redox reaction for Pt and GC working electrode materials at 25 °C and 1 bar.

The small variations in k_0 values between electrode materials with the Cu(I, II)-NH_3(aq) redox reaction suggest reactions may favor an outer-sphere charge transfer mechanism. In contrast, significant increases in k_0 were observed with Cl^-(aq) and Br^-(aq) ligands, indicating inner-sphere charge transfer mechanisms and possibly ligand-bridging.[57] In addition to the effects of the electrode material, ligand concentrations strongly altered reaction kinetics of the Br^-(aq), and Cl^-(aq) complexes but had little effect for NH_3(aq) complexes. Ligand-bridging has been observed with anion ligands that are both part of the oxidation and reduction metal ion coordination spheres, which can lead to enhanced charge transfer rates.[63] Still, these rate constants are 10 to 100 times larger than those observed with vanadium redox reactions (10μm s^{-1})[64], which indicates that these reactions are highly suitable for electrochemical energy conversion systems.[65]

3.3 Full cell performance

Thermal recharging of the system was mimicked by the addition of NH_3(aq) using a process developed previously.[2] Thermal regeneration has also been mimicked using ethylenediamine for Cu-based TRAB chemistries.[66] The addition of ammonia to the positive electrolyte substituted the weak field strength ligand, effectively reducing the potential of the Cu(I, II) redox reaction, thereby forming the electrolyte at the negative electrode. This procedure established the maximum thermally rechargeable potential possible for the solutions used (i.e., Assuming 100% recovery of ammonia).

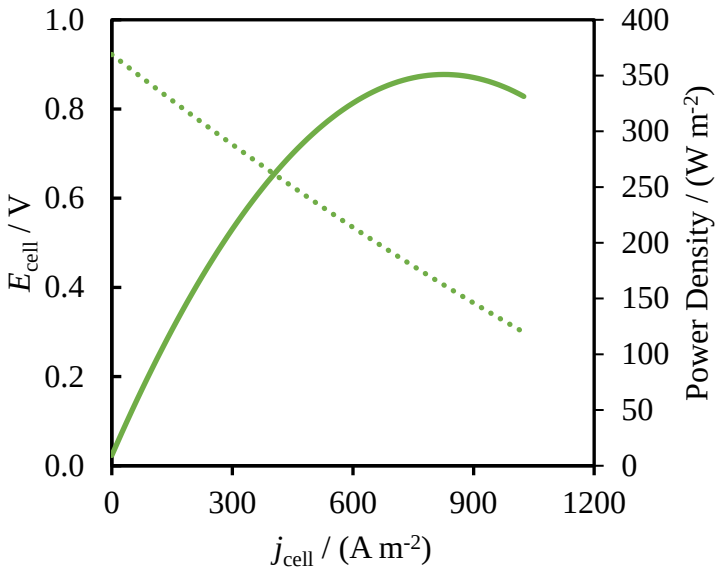

Figure 14. Power generation for the all-aq Cu-TRAB using a Nafion 115 membrane at 20 °C and 1 bar.

The fast kinetics and increased cell potentials resulted in high power densities from the all-aq TRAB. Relative to other flow batteries, such as the VRFB and Fe-Cr chemistries, the power densities obtained here of 123 to 350 W m^{-2} are comparable to the 100 to 600 W m^{-2} seen in previous chemistries.[67,68] Similar ranges have been obtained, 100 to 300 W m^{-2}, for some novel organic and aqueous flow battery chemistries.[69]

Cation and anion-selective membranes were used to investigate which solution, catholyte or the anolyte, was more susceptible to ligand crossover as well as the impacts on overall cell performance. Peak power densities obtained from the new flow battery chemistry were 350 W m^{-2} with N115, 240 W m^{-2} with N117, and 123 W m^{-2} with the AEM at 20 °C (**Figure 15**). The power density curves were largely dominated by ohmic losses regardless of the membrane tested. This was consistent with large j_0 values observed from the RDE data as well as conductivity measurements obtained from full cell tests. A 44% increase in membrane thickness between the N115 and N117 membranes equated to a 46% decrease in peak power density, with an increasingly negative impact on the power density as j_{cell} increased. Hence, a

proportional relationship between increased membrane thickness and a subsequent decrease in the power density of the cell is evident.

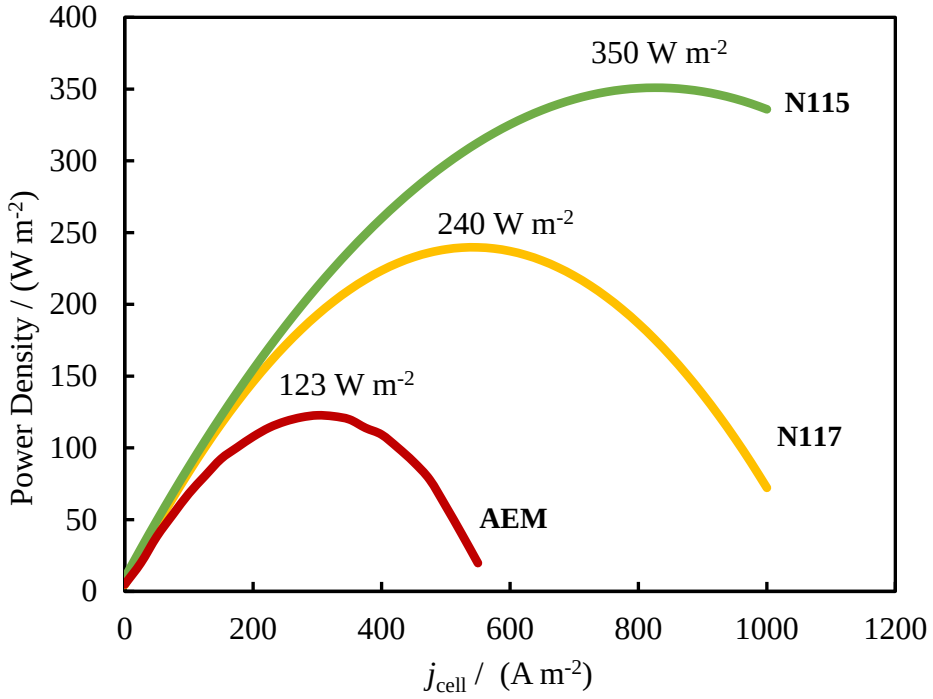

Figure 15. Power density curves obtained from the Br-NH3 all-aq TRB with Nafion 115 (green), Nafion 117 (yellow), and AEM membrane (red) at 25 °C and 1 bar with 0.5 mol kg^{-1} of total copper.

The coulombic efficiency was measured for the all-aq Cu(I, II) TRB was larger than those observed with copper metal TRABs. Electric charge-discharge cycling experiments were used to evaluate the coulombic efficiency of the full cell with Eq. 5. This contrasts with previous metal TRAB chemistries, where the coulombic efficiency of each electrode could be measured by simply measuring the change in mass of each electrode. The all-aq Cu-TRAB had a coulombic efficiency of 98% during the first cycle and then levelized

at about 90% with successive cycles. With efficiencies above 90%, this was a clear improvement over the typical 35% – 40% obtained with other metal copper-based systems (**Fig. 16**).[2,70]

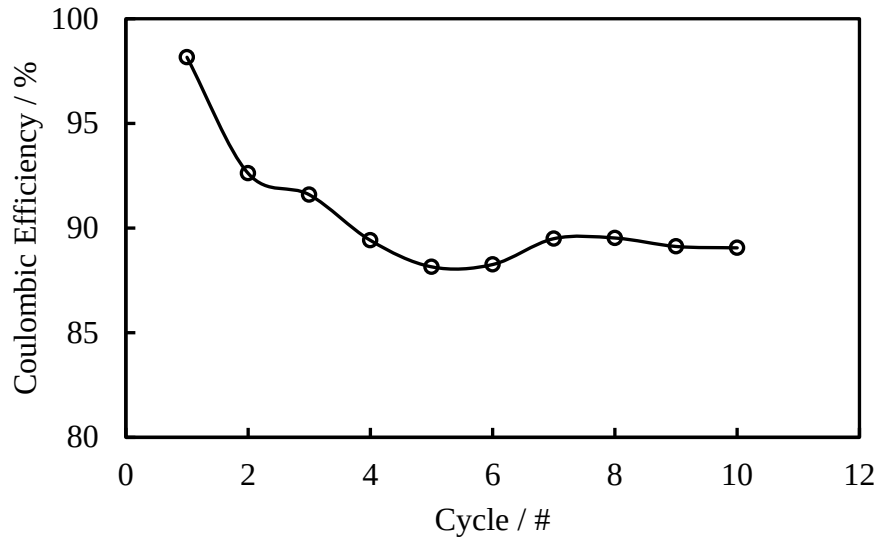

Figure 16. Coulombic efficiency of the all-aq Cu-TRAB after 10 cycles at 25 °C and 1 bar.

The sustained, high cell coulombic efficiency of the all-aq Cu-TRAB indicates that the electrochemical reactions in each half of the cell are fully reversible. The decrease in efficiency seen after the first cycle was likely due to NH_3 crossover through the membrane, which would decrease the performance of the catholyte over time. Evidence of NH_3 crossover was based on the catholyte solution slowly changing from brown to blue during cycling.

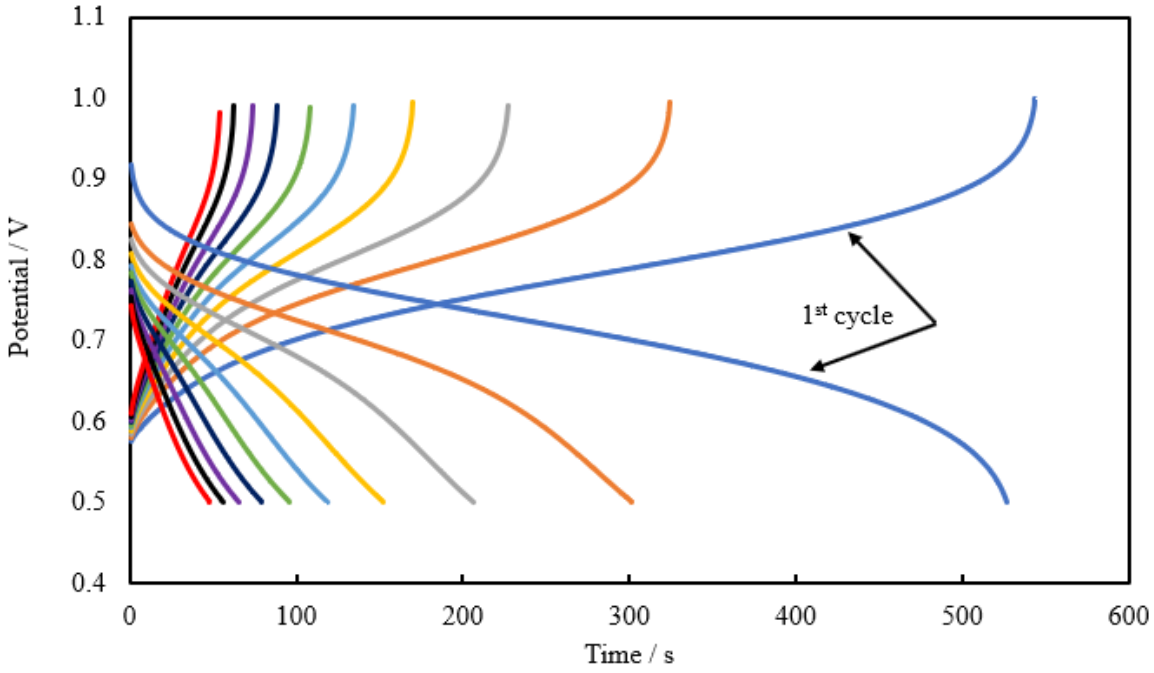

Figure 17. Charge and discharge curves for the Br-NH_3 all-Aq TRAB after 10 cycles at 25 ^{o}C and 1 bar with 0.5 mol kg^{-1} of total Cu.

However, this crossover will have minimal impact on the TRAB performance as the solutions are regenerated through thermal charging. While previous TRB publications were able to produce either high power cells or high coulombic efficiencies, few have been able to combine these two in the same chemistry. Therefore, the all-aq Cu-TRAB is unique because it can produce high power densities with high coulombic efficiencies using the same low-cost materials that have been used previously.

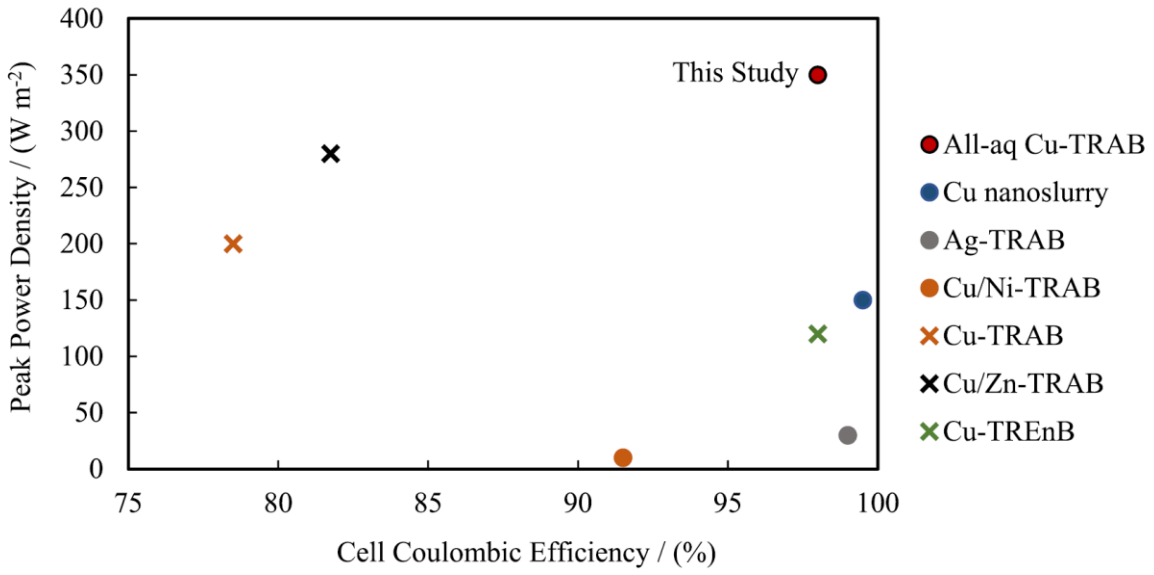

Figure 18. Comparison of peak power density and cell coulombic efficiency of different published TRB chemistries.[1–6]For metal-based batteries, the cell coulombic efficiency is an average of the reported electrode coulombic efficiencies. Circles indicate TRB chemistries that use reversible electrochemical reactions, and crosses indicate TRB chemistries with at least one irreversible electrochemical reaction.

Chapter 4 – Conclusions and Future Work

A new all-aqueous thermally regenerative redox flow battery was developed with favorable performance parameters relative to previous TRAB chemistries. RDE experiments obtained large equilibrium potentials with fast charge transfer kinetics. The strong field strength ligand NH_3(aq) resulted in a decrease of E_{eq} for the Cu (I, II) reaction to -47 ± 1 mV (vs SHE) whereas, the weak field strength ligands, Cl^-(aq) and Br^-(aq), increased the E_{eq} by 516 ± 7 mV and 638 ± 2 mV (vs SHE). Speciation calculations allowed for relatively accurate estimations of the E_{eq} potential shifts granted thermodynamic data is sound. Quantification of k_0 values indicated that these Cu(I, II) reactions were fast regardless of the ligand species. Charge transfer coefficients supported these findings as ligand concentration, ligand type, and surface materials only slightly changed α_c. Interestingly, the small variation in k_0 between Pt and GC working electrodes for NH_3(aq)-based complexes suggests that it followed an outer-sphere charge transfer

mechanism, whereas Cl^-(aq) and Br^-(aq) showed drastic differences in k_0 pointing to inner-sphere reaction mechanisms. Peak power densities obtained from the new battery chemistry were 350 W m^{-2} using a N115 membrane, exceeding previous TRAB technologies and in competition with the power densities obtained from conventional redox flow battery chemistries. Obtained coulombic efficiencies over 90% and an energy storage density of at least 9.4 Wh L^{-1} were significant improvements over existing chemistries, demonstrating promising advancements to the performance of TRABs.

As TRABs, like many other flow batteries, aim to provide energy storage for extended durations, analysis of cell longevity is essential. Although the all-aq Cu(I, II) TRAB is a promising development in TRAB technologies, future work should primarily focus on the cell life cycle analysis. Extended cycling tests would provide insights into the impact of species cross-over through the membrane on cell performance. Ideally, this would capture the operational lifetime of the all-aq Cu(I, II) TRAB and indicate whether solution distillation after each cycle is required. Hence, providing vital insights into the cost-effectiveness and overall cell efficiency. Analysis of the all-aq Cu(I, II) TRAB at elevated temperatures should also be a key focus of future studies. As a TRAB will be co-located with a large waste heat source, the operating temperature of TRABs can easily be increased above room temperature, which could significantly improve cell performance. Elevated temperatures can provide significant improvements to some processes like electrochemical kinetics and membrane conductivity but may have adverse impacts on solubility and standard cell potentials. Therefore, future TRAB studies could benefit from elevated temperature studies as elevated temperature operation may lead to an in increase in both energy storage density and power density of the all-aqueous TRAB.

References

1. Palakkal VM, Nguyen T, Nguyen P, et al. High Power Thermally Regenerative Ammonia-Copper Redox Flow Battery Enabled by a Zero Gap Cell Design, Low-Resistant Membranes, and Electrode Coatings. *ACS Appl Energy Mater*. 2020;3(5):4787-4798. doi:10.1021/acsaem.0c00400

2. Rahimi M, Kim T, Gorski CA, Logan BE. A thermally regenerative ammonia battery with carbon-silver electrodes for converting low-grade waste heat to electricity. *J Power Sources*. 2018;373(June 2017):95-102. doi:10.1016/j.jpowsour.2017.10.089

3. Rahimi M, D'Angelo A, Gorski CA, Scialdone O, Logan BE. Electrical power production from low-grade waste heat using a thermally regenerative ethylenediamine battery. *J Power Sources*. 2017;351:45-50.

4. Wang W, Shu G, Tian H, Huo D, Zhu X. A bimetallic thermally-regenerative ammonia-based flow battery for low-grade waste heat recovery. *J Power Sources*. 2019;424(December 2018):184-192. doi:10.1016/j.jpowsour.2019.03.086

5. Shi Y, Zhang L, Li J, Fu Q, Zhu X, Liao Q. Cu / Ni composite electrodes for increased anodic coulombic ef fi ciency and electrode operation time in a thermally regenerative ammonia- based battery for converting low-grade waste heat into electricity. *Renew Energy*. 2020;159:162-171. doi:10.1016/j.renene.2020.05.147

6. Maye S, Girault HH, Peljo P. Thermally regenerative copper nanoslurry flow batteries for heat-to-power conversion with low-grade thermal energy. *Energy Environ Sci*. 2020;13(7):2191-2199. doi:10.1039/d0ee01590c

7. Zeb K, Ali SM, Khan B, et al. A survey on waste heat recovery: Electric power generation and potential prospects within Pakistan. *Renew Sustain Energy Rev*. 2017;75:1142-1155.

doi:10.1016/J.RSER.2016.11.096

8. IEA. Energy Policies of IEA Countries. 2019, United States Review. *Iea*. Published online 2019:283.

9. Rahimi M, Straub AP, Zhang F, et al. Emerging electrochemical and membrane-based systems to convert low-grade heat to electricity. *Energy Environ Sci*. 2018;11(2):276-285. doi:10.1039/c7ee03026f

10. Braimakis K, Preißinger M, Brüggemann D, Karellas S, Panopoulos K. Low grade waste heat recovery with subcritical and supercritical Organic Rankine Cycle based on natural refrigerants and their binary mixtures. *Energy*. 2015;88:80-92. doi:10.1016/j.energy.2015.03.092

11. Brueske S, Sabouni R, Zach C, Andres H. *Manufacturing Energy and Carbon Footprints (2010 MECS)*.; 2012.

12. Ammar Y, Joyce S, Norman R, Wang Y, Roskilly AP. Low grade thermal energy sources and uses from the process industry in the UK. *Appl Energy*. 2012;89(1):3-20. doi:10.1016/J.APENERGY.2011.06.003

13. Enescu D. Thermoelectric Energy Harvesting: Basic Principles and Applications. *Green Energy Adv*. Published online January 21, 2019. doi:10.5772/INTECHOPEN.83495

14. Bianchini A, Pellegrini M, Saccani C. Thermoelectric cells cogeneration from biomass power plant. In: *Energy Procedia*. Vol 45. Elsevier Ltd; 2014:268-277. doi:10.1016/j.egypro.2014.01.029

15. Jung SM, Kwon J, Lee J, et al. Cu-Based Thermoelectrochemical Cells for Direct Conversion of Low-Grade Waste Heat into Electricity. *ACS Appl Energy Mater*. 2020;3(7):6383-6390. doi:10.1021/acsaem.0c00586

16. Wang W, Shu G, Tian H, Huo D, Zhu X. A bimetallic thermally-regenerative ammonia-based flow battery for low-grade waste heat recovery. Published online 2019. doi:10.1016/j.jpowsour.2019.03.086

17. Orr B, Singh B, Tan L, Akbarzadeh A. Electricity generation from an exhaust heat recovery system utilising thermoelectric cells and heat pipes. *Appl Therm Eng*. 2014;73(1):588-597. doi:10.1016/j.applthermaleng.2014.07.056

18. Rahimi M, Straub AP, Zhang F, et al. Emerging electrochemical and membrane-based systems to convert low-grade heat to electricity. *Energy Environ Sci*. 2018;11(2):276-285. doi:10.1039/C7EE03026F

19. Xie A, Popat SC. Electrochemical ammonia stripping from non-nitrified animal rendering wastewater. *Chem Eng J Adv*. 2020;3:100020. doi:10.1016/j.ceja.2020.100020

20. Deng G, Liang L, Jin Z, et al. Enhancing mass transport in direct methanol fuel cell by optimizing the microstructure of anode microporous layer. *AIChE J*. 2018;64(9):3519-3528. doi:10.1002/AIC.16193

21. Palakkal VM, Nguyen T, Nguyen P, et al. High Power Thermally Regenerative Ammonia-Copper Redox Flow Battery Enabled by a Zero Gap Cell Design, Low-Resistant Membranes, and Electrode Coatings. *ACS Appl Energy Mater*. 2020;3(5):4787-4798. doi:10.1021/acsaem.0c00400

22. Zhu X, Rahimi M, Gorski CA, Logan B. A Thermally-Regenerative Ammonia-Based Flow Battery for Electrical Energy Recovery from Waste Heat. *ChemSusChem*. 2016;9(8):873-879. doi:10.1002/cssc.201501513

23. Rahimi M. *Thermally Regenerative Ammonia Batteries For Converting Low-Grade Waste Heats to Electricity*.; 2017.

24. Zhang Y, Zhang L, Li J, et al. Performance of a thermally regenerative ammonia-based flow battery with 3D porous electrodes: Effect of reactor and electrode design. *Electrochim Acta*. 2020;331:135442. doi:10.1016/J.ELECTACTA.2019.135442

25. Gubler L. Membranes and separators for redox flow batteries. *Curr Opin Electrochem*. 2019;18:31-

36. doi:10.1016/J.COELEC.2019.08.007

26. Zhang F, Liu J, Yang W, Logan BE. A thermally regenerative ammonia-based battery for efficient harvesting of low-grade thermal energy as electrical power. *Energy Environ Sci*. 2015;8(1):343-349. doi:10.1039/c4ee02824d

27. Bard AJ, Parsons R, Jordan J. *Standard Potentials in Aqueous Solution*. Taylor & Francis; 1985.

28. Rahimi M, Kim T, Gorski CA, Logan BE. A thermally regenerative ammonia battery with carbon-silver electrodes for converting low-grade waste heat to electricity. *J Power Sources*. 2018;373(October 2017):95-102. doi:10.1016/j.jpowsour.2017.10.089

29. Crawford A, Viswanathan V, Stephenson D, et al. Comparative analysis for various redox flow batteries chemistries using a cost performance model. *J Power Sources*. 2015;293:388-399. doi:10.1016/J.JPOWSOUR.2015.05.066

30. Ha S, Gallagher KG. Estimating the system price of redox flow batteries for grid storage. *J Power Sources*. 2015;296:122-132. doi:10.1016/J.JPOWSOUR.2015.07.004

31. Wang W, Huo D, Tian H, Zhu X, Shu G. Temperature characteristics of a copper/zinc thermally-regenerative ammonia battery. *Electrochim Acta*. 2020;357:136860. doi:10.1016/j.electacta.2020.136860

32. Wang W, Tian H, Shu G, Huo D, Zhang F, Zhu X. A bimetallic thermally regenerative ammonia-based battery for high power density and efficiently harvesting low-grade thermal energy. *J Mater Chem A*. 2019;7(11):5991-6000. doi:10.1039/c8ta10257k

33. Dahl EW, Szymczak NK. Hydrogen Bonds Dictate the Coordination Geometry of Copper: Characterization of a Square-Planar Copper(I) Complex. *Angew Chemie - Int Ed*. 2016;55(9):3101-3105. doi:10.1002/ANIE.201511527

34. Pearson RG, Songstad J. Application of the Principle of Hard and Soft Acids and Bases to Organic

Chemistry. *J Am Chem Soc*. 1967;89(8):1827-1836. doi:10.1021/ja00984a014

35. Bhatt V. Basic Coordination Chemistry. *Essentials Coord Chem*. Published online January 1, 2016:1-35. doi:10.1016/B978-0-12-803895-6.00001-X

36. Martell AE, Hancock RD. *Metal Complexes in Aqueous Solutions*. Springer US; 1996. doi:10.1007/978-1-4899-1486-6

37. Patra SG, Datta D. Ligand field splitting in homoleptic tetrahedral d10 transition metal complexes. Spectrochemical series. *Comput Theor Chem*. 2018;1130:77-82. doi:10.1016/j.comptc.2018.03.012

38. Ellingsen DG, Horn N, Aaseth J. Copper. *Handb Toxicol Met*. Published online January 1, 2007:529-546. doi:10.1016/B978-012369413-3/50081-1

39. Rahimi M, Straub AP, Zhang F, et al. Emerging electrochemical and membrane-based systems to convert low-grade heat to electricity. *Energy Environ Sci*. 2018;11(2):276-285. doi:10.1039/c7ee03026f

40. Skyllas-Kazacos M, Cao L, Kazacos M, Kausar N, Mousa A. Vanadium Electrolyte Studies for the Vanadium Redox Battery—A Review. *ChemSusChem*. 2016;9(13):1521-1543. doi:10.1002/cssc.201600102

41. Hall DM, Akinfiev NN, LaRow EG, Schatz RS, Lvov SN. Thermodynamics and Efficiency of a CuCl(aq)/HCl(aq) Electrolyzer. *Electrochim Acta*. 2014;143:70-82. doi:10.1016/j.electacta.2014.08.018

42. Khurana S, Hall DM, Schatz RS, Lvov SN. Effect of Clamping Pressure and Temperature on the Performance of a CuCl(aq)/HCl(aq) Electrolyzer. *ECS Electrochem Lett*. 2015;4(4):F21-F23. doi:10.1149/2.0011504eel

43. Hall DM, Beck JR, Lvov SN. Electrochemical kinetics of the hydrogen reaction on platinum in

concentrated HCl(aq). *Electrochem commun*. 2015;57(1):74-77. doi:10.1016/j.elecom.2015.05.012

44. Hall DM, LaRow EG, Schatz RS, Beck JR, Lvov SN. Electrochemical Kinetics of CuCl(aq)/HCl(aq) Electrolyzer for Hydrogen Production via a Cu-Cl Thermochemical Cycle. *J Electrochem Soc*. 2015;162(1):F108-F114. doi:10.1149/2.0661501jes

45. Hall DM, Lvov SN. Modeling a CuCl(aq)/HCl(aq) Electrolyzer using Thermodynamics and Electrochemical Kinetics. *Electrochim Acta*. 2016;190:1167-1174. doi:10.1016/j.electacta.2015.12.184

46. Vanysek P. Electrochemical Series. In: *CRC Handbook of Chemistry and Physics*. ; 2020:5-88-to 5-89. doi:10.1007/1-4020-0613-6_5901

47. Johnson JW, Oelkers EH, Helgeson HC. SUPCRT92: A software package for calculating the standard molal thermodynamic properties of minerals, gases, aqueous species, and reactions from 1 to 5000 bars and 0 to 1000˚C. *Comput Geosci*. 1992;18:899-947.

48. Etschmann BE, Black JR, Grundler P V., et al. Copper(i) speciation in mixed thiosulfate-chloride and ammonia-chloride solutions: XAS and UV-Visible spectroscopic studies. *RSC Adv*. 2011;1(8):1554-1566. doi:10.1039/c1ra00708d

49. N. Lange A. Lange's handbook of chemistry (2005 ed.). New York: McGraw-Hill.

50. Hall DM, Grenier J, Duffy TS, Lvov SN. The Energy Storage Density of Redox Flow Battery Chemistries: A Thermodynamic Analysis. *J Electrochem Soc*. Published online July 2020. doi:10.1149/1945-7111/aba4e2

51. Kamau P, Jordan RB. Complex formation constants for the aqueous copper(I) - Acetonitrile system by a simple general method. *Inorg Chem*. 2001;40(16):3879-3883. doi:10.1021/ic001447b

52. OLI systems Inc. OLI Studio. Published online 2018.

53. Stricker EA. *Cuprous Bromide Electrochemistry and Its Application in a Flow Battery*.; 2019.

54. Dean JA. *Lange's Handbook of Chemistry*.; 1999.

55. Hathaway BJ, Tomlinson AG. Copper(u) ammonia complexes. *Coord Chem Rev*. 1970;5(iii):1-43.

56. Lvov SN. *Introduction to Electrochemical Science and Engineering*. 1st ed. CRC Press LLC; 2014.

57. Bard AJ, Faulkner LR. *Electrochemical Methods: Fundamentals and Applications*. 2nd ed. Wiley; 2000.

58. Ponce de León C, Frías-Ferrer A, González-García J, Szánto D a. A, Walsh FCC. Redox flow cells for energy conversion. *J Power Sources*. 2006;160(1):716-732. doi:10.1016/j.jpowsour.2006.02.095

59. Hall DM, Beck JR, Brand E, Ziomek-Moroz M, Lvov SN. Copper-Copper Sulfate Reference Electrode for Operating in High Temperature and High Pressure Aqueous Environments. *Electrochim Acta*. 2016;221:96-106. doi:10.1016/j.electacta.2016.10.143

60. Dhillon S, Kant R. Theory for electrochemical impedance spectroscopy of heterogeneous electrode with distributed capacitance and charge transfer resistance. *J Chem Sci*. 2039;129(8):1277-1292. doi:10.1007/s12039-017-1335-x

61. Ahmad Z. *Principles of Corrosion Engineering and Corrosion Control*. Elsevier Ltd; 2006. doi:10.1016/B978-0-7506-5924-6.X5000-4

62. Kim J, Park H. Experimental analysis of discharge characteristics in vanadium redox flow battery Experimental analysis of discharge characteristics in vanadium redox flow battery A R T I C L E I N F O. *Appl Energy*. 2017;206:451-457. doi:10.1016/j.apenergy.2017.08.218

63. Haim A. Role of the Bridging Ligand in Inner-Sphere Electron-Transfer Reactions. *Prog Inorg Chem*. 1959;1(3):2635. Accessed May 28, 2020. https://pubs.acs.org/sharingguidelines

64. Roznyatovskaya N, Noack J, Pinkwart K, Tübke J. Aspects of electron transfer processes in vanadium redox-flow batteries. *Curr Opin Electrochem*. 2020;19:42-48. doi:10.1016/J.COELEC.2019.10.003

65. Liu M, Xiang Z, Deng H, et al. Electrochemical Behavior of Vanadium Redox Couples on Carbon Electrode. *J Electrochem Soc*. 2016;163(10):H937-H942. doi:10.1149/2.0441610jes

66. Rahimi M, Zhu L, Kowalski KL, et al. Improved electrical power production of thermally regenerative batteries using a poly(phenylene oxide) based anion exchange membrane. *J Power Sources*. 2017;342:956-963. doi:10.1016/j.jpowsour.2017.01.003

67. Zeng YK, Zhou XL, An L, Wei L, Zhao TS. A high-performance flow-field structured iron-chromium redox flow battery. *J Power Sources*. 2016;324:738-744. doi:10.1016/j.jpowsour.2016.05.138

68. Aaron DS, Liu Q, Tang Z, et al. Dramatic performance gains in vanadium redox flow batteries through modified cell architecture. *J Power Sources*. 2012;206:450-453. doi:10.1016/j.jpowsour.2011.12.026

69. Chen H, Cong G, Lu Y. Recent Progress in Organic Redox Flow Batteries: Active Materials, Electrolytes and Membranes. *J Energy Chem*. 2018;27:1304-1325. doi:S2095495617311051

70. Zhang F, LaBarge N, Yang W, Liu J, Logan BE. Enhancing Low-Grade Thermal Energy Recovery in a Thermally Regenerative Ammonia Battery Using Elevated Temperatures. *ChemSusChem*. 2015;8(6):1043-1048. doi:10.1002/cssc.201403290